IEEE Access
Multidisciplinary | Rapid Review | Open Access Journal

Received 9 August 2022, accepted 2 September 2022, date of publication 5 September 2022, date of current version 14 September 2022.

Digital Object Identifier 10.1109/ACCESS.2022.3204648

RESEARCH ARTICLE

System Development of Calibration-Free 20.7-Bit Chipless RFID Without Iterative Optimization of Tag Configurations

JIA-WEN HSU, FEI-PENG LAI, AND YEN-SHENG CHEN, (Member, IEEE)
Department of Electronic Engineering, National Taipei University of Technology, Taipei 10608, Taiwan

Corresponding author: Yen-Sheng Chen (yschen@ntut.edu.tw)

This work was supported by the Ministry of Science and Technology, Taiwan, under Contract MOST 111-2221-E-027-047-MY2.

ABSTRACT Earlier studies have improved the data capacity of frequency-coded chipless radiofrequency identification (RFID) to 100 bits, but these high-density tags may suffer from two limitations, including the design complexity for billions of tags and an additional procedure for measuring clutter. In this paper, a calibration-free chipless RFID system with 20.7-bit capacity is proposed; moreover, the design of the 1.68 million tags is highly efficient, preventing individual and iterative optimization for such large numbers of configurations. These distinct features are obtained by integrating the signal processing of reader and the resonance synthesis of tags. The signal processing employs short-time Fourier transform (STFT) and enhanced filtering to achieve calibration-free detection. The resonance synthesis features minimized numbers of geometric parameters, reduced mutual coupling between resonators, and response surface models for the resonant frequency to realize noniterative optimization. The proposed system is validated by three approaches. First, residual plots indicate that the range of residuals is confined to the average bandwidth of frequency slots. Second, 36 IDs are sampled and automatically transformed into chipless tags. The measured reliability of four bands is as high as 100%, 95.0%, 98.3%, and 93.9%, respectively. Finally, the parameterization of signal processing is validated by time-frequency analysis and reliability.

INDEX TERMS Frequency response, radiofrequency identification, resonator, robustness, signal detection.

I. INTRODUCTION

Chipless radiofrequency identification (RFID) is an emerging Internet of Things (IoT) technology. The tag of chipless RFID eliminates a microchip, thereby reducing the cost from conventional RFID. While the data can be encoded using frequency [1], [2], [3], [4], time [5], [6], or hybrid signatures [7], [8], frequency-coded chipless RFID has shown potential of capacity enhancement. The data capacity can reach as high as 28.5 bits [1], 31 bits [2], 40 bits [3], or even 100 bits [4], indicating that billions of IDs are recorded by chipless tags.

However, the high-capacity frequency-coded chipless RFID has risen to two challenges. First, the chipless tag is comprised of multiple resonators with numerous geometric parameters, such as closed loops [1], U-shaped strips [2], [3], and crossed dipoles [4]. Mutual coupling between resonators makes the synthesis of resonant frequencies require performing iterative full-wave simulations. As billions of chipless tags need to be optimized to accommodate individual IDs, accomplishing the full RFID system is time-consuming. Thus, a synthesis technique without performing iterative simulation runs is urgent for high-capacity chipless tags [9].

Second, the frequency signature of earlier high-capacity systems is radar cross sections (RCS) [1], [2], [3], [4], which require measuring the response of clutter. As items to be attached have distinct responses of clutter, this additional procedure makes the use of RCS impractical in real-world applications. Although several calibration-free detections have been studied [10], [11], [12], [13], [14], [15], [16], [17], [18], [19], [20], these techniques did not address high data capacity exceeding 20 bits or the noniterative optimization of chipless tags.

In particular, the characteristics of earlier calibration-free techniques are summarized in Table 1 [10], [11], [12],

The associate editor coordinating the review of this manuscript and approving it for publication was S. M. Rezaul Hasan.

TABLE 1. Comparison of characteristics for calibration-free detection methods.

No.	Calibration -free technique	Frequency range (GHz)	Data capacity (bit)	Design technique for tags	Statistical evaluation of read reliability?
[10]	STFT with enhanced filtering	2.0–4.0	8	Iterative Tuning	Yes
[11]	STFT	3.0–7.0	8	Iterative Tuning	No
[12]	STFT	3.0–6.0	13	Iterative Tuning	No
[13]	STFT with MPM	3.0–7.0	8	Iterative Tuning	Yes
[14]	STFT with MPM	3.0–6.0	12	Iterative Tuning	Yes
[15]	STFT	2.0–6.0	22.1	Iterative Tuning	No
[16]	Difference between orthogonally -scattered components	2.0–6.0	3	Iterative Tuning	No
[17]	Difference between orthogonally -scattered components	2.0–8.0	10	Iterative Tuning	No
[18]	Windowing based on extraction of modes	4.6–5.4	4	Iterative Tuning	No
[19]	Assuming zero clutter	7.0–11.0	16	Iterative Tuning	No
[20]	Pulse distortion approach	3.1–10.6	4 (Potentially 37)	Iterative Tuning	No
This study	STFT with enhanced filtering	2.0–6.0	20.7	Noniterative synthesis (RSM)	Yes

[13], [14], [15], [16], [17], [18], [19], [20]. Most of the calibration-free detections feature short-time Fourier transform (STFT) for backscattering signals [10], [11], [12], [13], [14], [15]. To improve the time-frequency windowing resolution, several schemes are integrated to STFT, such as enhanced filtering [10] and matrix pencil methods (MPM) [13], [14]. Another technique encodes information using orthogonally-polarized components [16], [17]. While detecting the two backscattering components comprises the response of clutter, evaluating the difference between them is expected to cancel out the clutter, thereby enabling a normalization-free manner. In addition, the resonance can be extracted without calibration by a special time-frequency reconstruction approach [18], analyzing the transfer functions of structural mode and tag mode as well as the propagation channel. Another study employs only the amplitude of fields, detecting IDs without calibration by assuming the amplitude of clutter is insignificant [19]. A multicarrier detection scheme is proposed to process the backscattering signals directly in the time domain [20]. When the transmitted signal bandwidth and the rejection level of a low pass filter are optimized, theoretically, this scheme can implement 37 carrier signals, which indicates that the reader can detect 37 bits.

Table 1 also presents the data capacity, the design technique of tags, and the evaluation scheme of experimental results. Only two studies demonstrate capacity greater than 16 bits [15], [19]. While the multicarrier detection scheme has a maximum achievable capacity of 37 bits, the prototype validates the concept by a 4-bit system [20]. When the number of ID combinations is as high as thousands [19], millions [15], or even billions [20], converting all the IDs to tag geometry requires significant time and efforts, if the tags are designed by iterative tuning. For example, the calibration-free tag has been developed by 16 dipole arrays backed with conductor [19]. The length and separation of these dipoles require iterative optimization, for closely adjacent resonances may be merged due to the mutual coupling. As illustrated in Table 1, a noniterative synthesis technique is lacking for the calibration-free and high-capacity tags. Besides, only few literatures have evaluated the calibration-free detection in a statistical manner [10], [13], [14], which computes the portion of successful detection out of a large number of tests. This evaluation method has gathered great attentions to the implementation of chipless RFID in real-world environments [21].

The goal of this paper is to develop a high-capacity and calibration-free system without performing iterative optimization for the tags. In addition to our preliminary study that encodes 22.1 bits only in simulation [15], this paper constructs the highest overall data capacity with calibration-free detection; more importantly, the tags are designed by the noniterative synthesis. 1.68 million tags can be determined by mathematical expressions, instead of iterative full-wave simulation. The proposed technique consists of reader signal processing based on STFT and specific tags created using response surface models (RSMs) [22]. By reducing the number of geometric parameters of one resonator and mutual coupling between resonators, the resonant frequencies can be synthesized independently. The capability of the proposed system will be demonstrated through residual plots, the measurement of a 20.7-bit system over 2.0–6.0 GHz, and the time-frequency analysis. The impact of the study is to advance the chipless RFID to real-world implementation with two-fold performance enhancements. 1.68 million IDs can be converted to tag configurations in an efficient way, and their information can be extracted without performing calibration runs.

II. SYSTEM ARCHITECTURE

The proposed chipless RFID is illustrated by the setup of communication system, hardware, and software. In particular, the setup of communication system is explained by the frequency spectrum and a new encoding scheme that improves guardbands. The hardware and software are

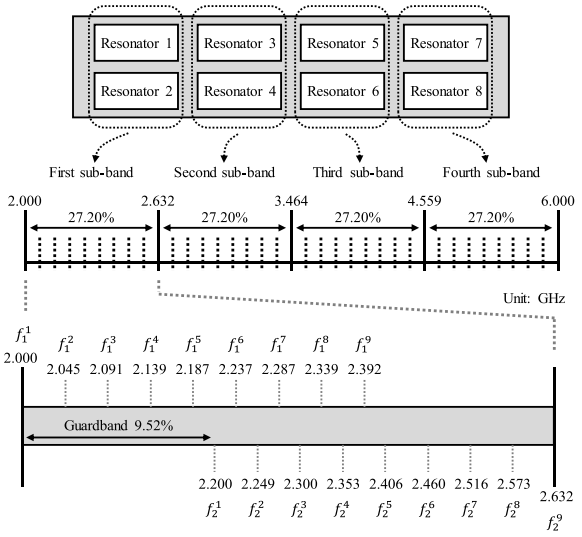

FIGURE 1. Frequency spectrum of the 20.7-bit frequency-coded chipless RFID system.

reported by the resonator of a tag and reader signal processing, respectively.

A. SETUP OF COMMUNICATION SYSTEM

Figure 1 shows the spectrum of the 20.7-bit frequency-coded chipless RFID. The frequency range is divided into four sub-frequency bands, including 2.000–2.632 GHz, 2.632–3.464 GHz, 3.464–4.559 GHz, and 4.559–6.000 GHz. The four sub-frequency bands show different bandwidths in the linear-scale system, but they demonstrate an identical factional bandwidth, 27.2%. The use of 2.0–6.0 GHz is to meet the tradeoff between the bandwidth of a resonator and the resolution of printed circuit board (PCB) manufacturing, as using ultra-wideband (UWB) requires a PCB resolution less than 0.1 mm, which exceeds our resource. Each sub-frequency band implements a revised frequency shift encoding scheme. Conventional frequency shift encoding employs one resonance over several frequency slots [23]; however, the revised one uses two resonances in a sub-frequency band.

Figure 2 is the encoding scheme in the first sub-frequency band, denoted by F_1. Two resonators are responsible for the encoding in F_1, and their frequencies are denoted by f_1^i and f_2^j, respectively. Their combination results in one unique code in this band. More explicitly, f_1^i (GHz)$\in$ {2.000, 2.045, 2.091, 2.139, 2.187, 2.237, 2.287, 2.339, 2.392}, f_2^j (GHz)$\in$ {2.200, 2.249, 2.300, 2.353, 2.406, 2.460, 2.516, 2.573, 2.632}, i, $j = 1, 2, \ldots, 9$, and $i < j$. For example, the third code in F_1 employs $(f_1^1, f_2^4) = (2.000$ GHz, 2.353 GHz); thus, this code can be identified by two resonators designed at 2.000 GHz and 2.353 GHz, respectively. Similarly, the twenty-seventh code in F_1 employs $(f_1^5, f_2^6) = (2.187$ GHz, 2.460 GHz); the code can be detected by two resonators operated at 2.187 GHz and 2.460 GHz, respectively. As a result, 36 codes are present in F_1 by confining $i < j$.

f_2^j(GHz) \ f_1^i (GHz)	f_1^1 (2.000)	f_1^2 (2.045)	f_1^3 (2.091)	f_1^4 (2.139)	f_1^5 (2.187)	f_1^6 (2.237)	f_1^7 (2.287)	f_1^8 (2.339)	f_1^9 (2.392)
f_2^1 (2.200)									
f_2^2 (2.249)	1								
f_2^3 (2.300)	2	9							
f_2^4 (2.353)	3	10	16						
f_2^5 (2.406)	4	11	17	22					
f_2^6 (2.460)	5	12	18	23	27				
f_2^7 (2.516)	6	13	19	24	28	31			
f_2^8 (2.573)	7	14	20	25	29	32	34		
f_2^9 (2.632)	8	15	21	26	30	33	35	36	

FIGURE 2. Detailed implementation for the proposed coding in the first sub-frequency band.

In addition, the frequency separations for the third and the twenty-seventh codes are 353 MHz and 273 MHz, respectively. In fact, the frequency separations shown in Figure 2 guarantee a frequency separation of more than 200 MHz. These frequency separations serve the coding as a guardband, which extends the range of adjacent resonances; accordingly, the risk in frequency aliases is reduced.

Following this rule, the second sub-frequency band, F_2, employs two resonances at (f_3^i, f_4^j), where f_3^i(GHz) $\in$ {2.632, 2.691, 2.752, 2.815, 2.879, 2.944, 3.011, 3.079, 3.149}, f_4^j(GHz) $\in$ {2.895, 2.961, 3.028, 3.096, 3.167, 3.238, 3.312, 3.387, 3.464}, $i, j = 1, 2, \ldots, 9$, and $i < j$. Accordingly, extra 36 codes can be assigned in F_2, and the adjacent resonances in each code are separated by more than 200 MHz. Likewise, the third and fourth sub-frequency bands implement F_3 (GHz) $= (f_5^i, f_6^j)$ and F_4 (GHz) $= (f_7^i, f_8^j)$, respectively, where $f_5^i \in$ {3.464, 3.542, 3.623, 3.705, 3.789, 3.875, 3.962, 4.052, 4.144}, $f_6^j \in$ {3.810, 3.896, 3.985, 4.075, 4.168, 4.262, 4.359, 4.457, 4.559}, $f_7^i \in$ {4.559, 4.662, 4.768, 4.876, 4.986, 5.099, 5.215, 5.333, 5.454}, $f_8^j \in$ {5.014, 5.128, 5.244, 5.363, 5.485, 5.609, 5.736, 5.867, 6.000}, indices $i, j = 1, 2, \ldots, 9$, and $i < j$. As each band has 36 data combinations, the four bands provide $36^4 = 1{,}679{,}616 \approx 2^{20.7}$ ID strings.

The proposed encoding improves the detection reliability, and it utilizes frequency resource more efficiently. The frequency separation is ensured to be greater than 200 MHz, which contributes to sufficient guardbands. In contrast, the conventional frequency shift encoding requires 7 frequency slots for 8 resonators ($8^7 = 21$ bits); accordingly, adjacent frequency slots are separated by only 45 MHz. This indicates that the proposed encoding reduces the potential aliases due to closely adjacent resonances.

B. RESONATOR

To serve the revised frequency shift encoding, a chipless tag employs 8 resonators. The resonator selected is an L-shaped slot, the topology of which is shown in Figure 3. The L-shaped slot is fabricated on a 1.524-mm-thick

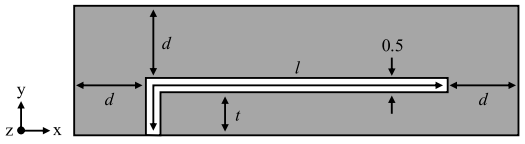

FIGURE 3. Proposed resonator and the associated geometric parameters (unit: mm).

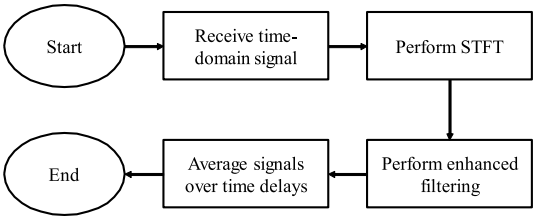

FIGURE 4. Procedure of the proposed calibration-free detection.

RO4003C substrate (dielectric constant $\varepsilon_r = 3.55$ and loss tangent $\tan\delta = 0.0027$). The geometric parameters include the identical distance to the left, right, and upper edges of the substrate, d, the distance to the lower edge, t, and the total length of the slot, l. As the L-shaped slot is not backed with conductor, the proposed system addresses items with a low dielectric constant and a thin layer, and it is not applicable for challenging objects such as metal or water.

The three geometric parameters influence the resonant frequency, thereby controlling the ID. Summarizing 8 resonators, the number of design factors for tuning IDs increases significantly. This makes the synthesis of resonant frequencies rely on iterative optimization. Considering 1.68 millions of IDs need to be accommodated, repeating the iterative optimization for each tag requires unacceptably long time. Accordingly, a noniterative synthesis technique for the 1.68 millions of IDs is emerging.

C. READER SIGNAL PROESSING

The reader signal processing employs STFT featuring enhanced filtering. While STFT has been considered as an effective calibration-free technique [10], [11], [12], [13], [14], [15], the algorithm implemented in this system comprises the standard STFT operation, time gating, and the enhanced filtering on time-frequency spectrograms.

Figure 4 shows the proposed calibration-free detection. The process starts by transmitting frequency modulated continuous waveform (FMCW) signals from a reader. The reader readily measures the backscattering cross-polarized fields of a tag. These backscattering fields comprise the reflection at the feeding port, the late response of the clutter, and the desired encoding information of the tag. The time gating is performed to remove the antenna reflection and the late response of the clutter, which leads to a time-domain signal, $x(t)$. An example of $x(t)$ is shown in Figure 5(a). Next, a window function, $w(t)$, with a length of T_w performs

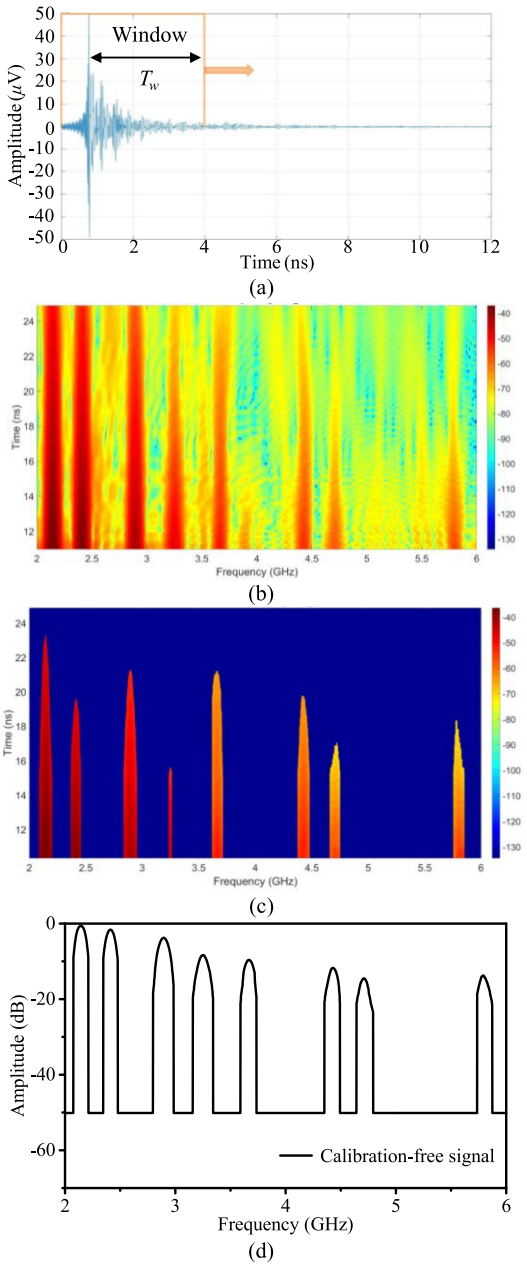

FIGURE 5. An example of the calibration-free detection with enhanced filtering. (a) The original time-domain response, (b) the associated time-frequency plot, (c) the result after enhanced filtering, and (d) the output decoded by a reader.

convolution integral to $x(t)$:

$$S(f,t) = \int_{-\infty}^{+\infty} x(t)\, w(\tau - t) e^{-j2\pi ft} d\tau \qquad (1)$$

where $S(f, t)$ is the output in terms of a time-frequency spectrogram, τ is delay time across the window function $w(t)$, and t and f are time and frequency, respectively. This STFT operation leads to the time-frequency spectrogram, as shown in Figure 5(b).

The window function and its length are the most crucial factors in the time-frequency analysis. The window

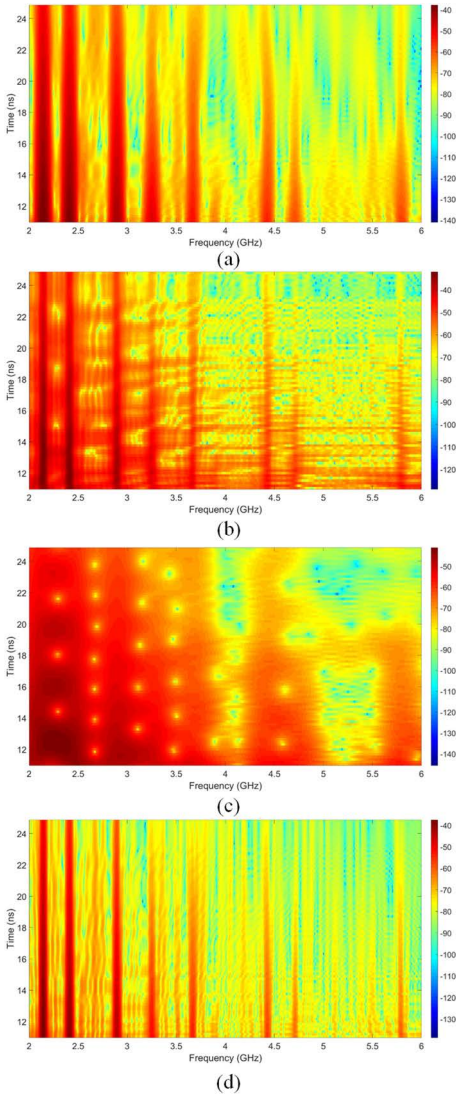

FIGURE 6. Parameterization of the proposed technique. (a) Gaussian window. (b) Rectangular window. (c) $T_W = 4.8$ ns. (d) $T_W = 35.2$ ns.

function implemented in this study is a Hamming function with $T_w = 17.6$ ns. To demonstrate the effect of these parameters, Figures 6(a) and 6(b) demonstrate the results of Gaussian and rectangular windows, respectively. The Hamming and Gaussian windows result in good resolution. The strengths of signal are comparable, and the resonances can be identified clearly. On the other hand, the rectangular window causes blur amplitudes. The reliability may be greatly reduced due to the confounding resonances. In addition, Figures 6(c) and 6(d) depict the results for short and long T_w, respectively, which lead to opposite strengths for the signal. When $T_w = 4.8$ ns, the short window length causes aliasing of information, where the magnitudes are too large to be distinguished. When $T_w = 35.2$ ns, on the other hand, the magnitudes are overly reduced, whereas the resolution becomes insufficient, especially for the resonance at high frequencies.

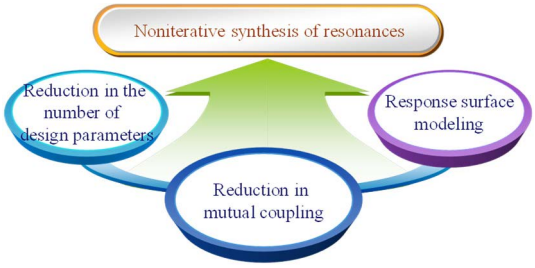

FIGURE 7. Crucial elements for calibration-free and noniterative synthesis of resonances.

Following the STFT process, the proposed calibration-free technique performs the enhanced filtering to distinguish non-resonance components. First, the maximum magnitude is detected, and those signals with a magnitude that is one tenth of the maximum are removed. Afterward, the antenna reflection of the input port is dependent on both time and frequency. The reflection at a lower frequency lasts longer; in contrast, the reflection at a higher frequency continues for a shorter time. When averaging the signal over τ, this bias incurs decreased reliability. Thus, the proposed filtering mechanism identifies this influence and rejects those reflection components. This results in an enhanced time-frequency spectrogram, as shown in Figure 5(c). This time-frequency plot provides clarified resonances; more importantly, taking the average of $S(f, t)$ over t is not sensitive to the selected region of t, and thus the subjective judgment for the interval of delay time can be prevented.

With the enhanced time-frequency spectrogram at hand, the calibration-free technique computes average frequency responses over signal durations, which are output as the final frequency signature, as shown in Figure 5(d). As such, even though the clutter is not calibrated, the resonances of the chipless tag can be identified clearly.

III. NONITERATIVE SYNTHESIS OF RESONANCES

Although the online detection issue is resolved by the calibration-free technique, the offline design problem, namely, constructing the 20.7-bit system and synthesizing 1.68 million tags, requires a noniterative synthesis method. Figure 7 shows the crucial elements of the proposed method. First of all, there are three design parameters for one resonator. More numbers of parameters introduce higher-order interactions, which increase model complexity. Second, arranging 8 resonators together further increases the overall number of design parameters, unless they have insignificant mutual coupling that leads to independent synthesis. Third, the goal of the proposed technique is to build up RSMs, which are the function of the solitary design parameter. These models should fully explain the relationship between a resonant frequency and that design parameter. Only by integrating the three elements, the 1.68 million tags can be designed without iterative tuning or optimization.

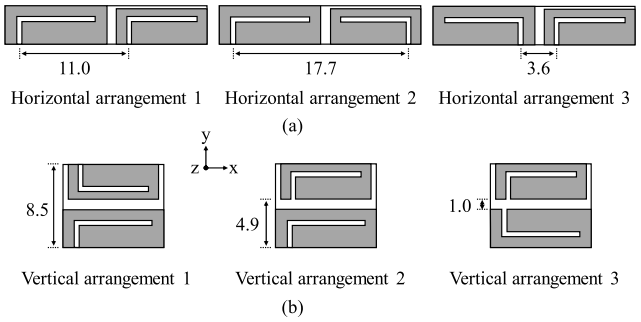

FIGURE 8. (a) Horizontal and (b) vertical arrangements for two resonators (unit: mm).

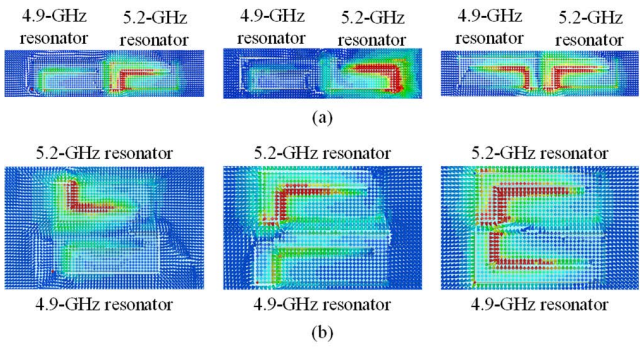

FIGURE 9. Field distributions of (a) horizontal and (b) vertical arrangements at 5.20 GHz.

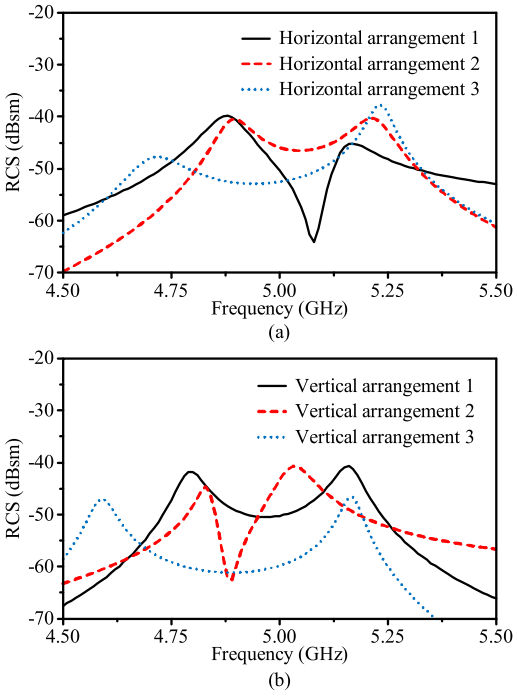

FIGURE 10. Simulated RCS for two resonators that are (a) horizontally or (b) vertically arranged.

A. REDUCTION IN THE NUMBER OF DESIGN PARAMETERS

The first issue, the reduction in the number of design parameters, is solved by the scaling as the function of frequency. We set l as the solitary parameter, determining d and t based on the interpolation between a resonant frequency and the fractional bandwidth. In particular, d and t are varied over 5.0–0.7 mm and 3.0–2.0 mm, respectively, as the resonant frequency is synthesized over 2.0–6.0 GHz. In this way, only l is cast into the explanatory variable of the RSM.

B. REDUCTION OF MUTUAL COUPLING

Although the frequency of a resonator is determined by only one variable, a tag consists of 8 resonators, and the mutual coupling between resonators causes frequency shifts and the incorrect output of IDs. Thus, the next step is to develop a layout with minimized mutual coupling between the resonators.

Figure 8 shows potential 6 arrangements for adjacent resonators, including horizontal and vertical placements with different distances between the open-ended points. For demonstration purposes, the two L-shaped slots are designed to provide an individual resonance at 4.90 GHz and 5.20 GHz, respectively. When the two resonators are put together, horizontal arrangements 2 and 3 illustrate the longest and shortest separations between the open ends, respectively. On the other hand, vertical arrangements 1 and 3 depict the longest and shortest separations, respectively.

The test of optimum layout is carried out using 5.2-GHz y-polarized plane waves, which impinge on the two L-shaped slots. Figure 9 shows the simulated x-polarized electric field distributions. Ideally, only the 5.2-GHz resonator echoes with the incident waves; however, in the horizontal arrangement 3, the 4.9-GHz resonator also responses with strong magnitudes. This effect is caused by the mutual coupling, and the undesired resonance modifies the current pathway and the associated length, which further result in a frequency shift and detuning. The horizontal arrangement 1 also incurs mutual coupling, with medium strong magnitudes. Similarly, the vertical arrangement 3, which employs the narrowest separation between the open ends, suffers from significant mutual coupling. The extended current pathway causes a frequency shift for 5.2-GHz encoding information. Accordingly, the mutual coupling makes the synthesis of 8 resonances challenging unless the open ends are separated widely.

To verify the results, the 6 arrangements are further illuminated by broadband plane waves, and the RCS spectrums are simulated and shown in Figure 10. The resonator originally operated at 4.9 GHz has frequency shifts of 16 MHz, 2 MHz, and 197 MHz, for the three horizontal arrangements, respectively, whereas the frequency shifts for the three vertical arrangements are 11 MHz, 7 MHz, and 310 MHz. Accordingly, the open ends are required to be set apart as far as possible.

Based on these design rules, the proposed tag geometry with minimized mutual coupling is depicted in Figure 11. The dimensions are 63.1 $\times$ 56.9 mm^2. The 8 L-shaped slots have divided ground planes to enhance isolation, and the adjacent open-ended points are separated as wide as possible.

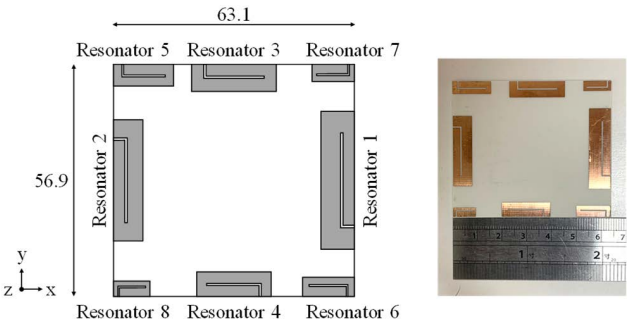

FIGURE 11. Topology of the proposed chipless RFID tag (unit: mm).

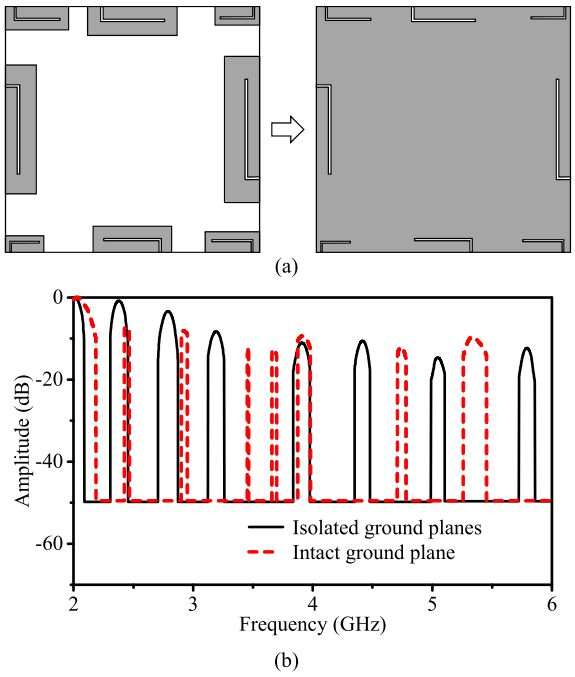

FIGURE 12. (a) Tag geometry without isolated ground planes and (b) the detection result.

The divided ground plane is important for tuning the resonance independently. An example is the tag with resonances at 2.01 GHz, 2.38 GHz, 2.79 GHz, 3.19 GHz, 3.91 GHz, 4.39 GHz, 5.05 GHz, and 5.79 GHz. When the ground planes are united, as shown in Figure 12, the resonances are shifted to 2.03 GHz, 2.44 GHz, 2.92 GHz, 3.46 GHz, 3.67 GHz, 3.92 GHz, 4.72 GHz, and 5.34 GHz. The encoding resonances of the intact ground plane feature frequency shifts due to the mutual coupling. As a result, the synthesis of resonances cannot be performed using individual resonators, thereby increasing the complexity in the RSMs.

C. RESPONSE SURFACE MODELING

The last step of the proposed technique is to formulate RSMs for the solitary design parameter, l. This step is based on regression analysis. A training dataset is constructed to predict the behavior of test data [24], [25].

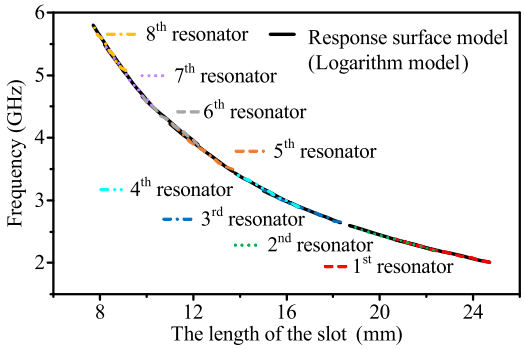

FIGURE 13. Comparison between RSMs and the training dataset.

The response surface modeling consists of two phases. The phase one is to analyze the resonant frequency of a training dataset. For each resonator, 10 lengths are uniformly selected, and their resonant frequencies are simulated. With the results at hand, the phase two constructs mathematical models and selects the one with respect to minimum mean square error (MMSE). In the problem of resonant frequencies, five models are fitted to the training data, including logarithm, power, exponential, and first-order and second-order polynomial functions. The capability of the model is examined by R^2, which indicates the percentage of the variance in the resonant frequency that l can explain. As a result, the logarithm model introduces a highest average R^2 of 0.99:

$$f_k(l) = a_k \times \ln(l) + b_k(\text{GHz}), \tag{2}$$

where $f_k(l)$ is the frequency of the k^{th} resonator with a length of l mm, index $k = 1, 2, \ldots, 8$, and the estimated coefficients are $a_1 = -2.048$, $b_1 = 8.575$, $a_2 = -2.206$, $b_2 = 9.056$, $a_3 = -2.551$, $b_3 = 10.059$, $a_4 = -3.001$, $b_4 = 11.309$, $a_5 = -3.486$, $b_5 = 12.585$, $a_6 = -3.469$, $b_6 = 12.573$, $a_7 = -4.424$, $b_7 = 14.795$, $a_8 = -4.524$, and $b_8 = 15.035$.

The 8 RSMs and the training dataset are shown in Figure 13. Good agreement can be observed between the results predicted by (2) and the training data, confirming the significant R^2 obtained (99%). Thus, the resonant frequency can be predicted using an expression (2), instead of iterative optimization or tuning from full-wave simulation.

Integrating the 3 characteristics, 8 resonators can be designed independently, and their solitary design parameter, l, is determined by (2). An ID can be converted into a tag configuration almost instantly. Even though 1.68 million tags need to be coped with, the proposed noniterative synthesis method greatly reduces the computational time from iterative optimization, and this makes 20.7-bit chipless RFID feasible in the real world.

IV. RESULTS

The capability of the proposed calibration-free 20.7-bit chipless RFID is examined through three aspects, including model prediction, reliability, and the parameterization in signal processing.

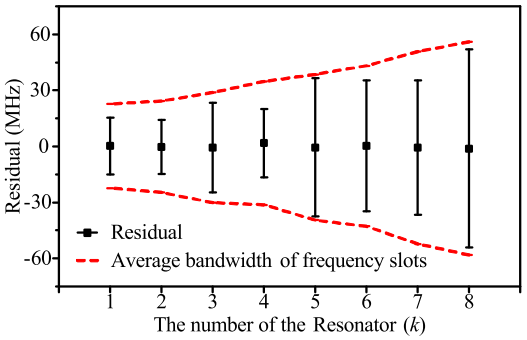

FIGURE 14. Estimated mean and range of residuals for each resonator.

A. VALIDITY OF RESPONSE SURFACE MODELS

First of all, the most important scheme of the proposed high-capacity system is free from iterative optimization for millions of tags. While Figure 14 indicates good agreement visually, the models should be validated by quantitative results.

The residual of models analyzes the quantitative relationship, computed from the difference between model predictions and simulated results. For each resonator, the 10 residuals are evaluated, and the range is compared with the bandwidth of each frequency slots. The results are shown and compared in Figure 14. Note that the proposed communication system aims at an identical fractional bandwidth, so the bandwidth in the linear scale increases with frequency. While each resonator depicts different residuals, the ranges are enclosed by the average bandwidth of the frequency slots. In addition, the average of the residual closely follows zero. This indicates that the estimated mean of errors is zero and the maximum deviation is still confined in the bandwidth of any frequency slots, lending validity to the prediction capability of the RSMs.

B. RELIABILITY

Next, the proposed 20.7-bit calibration-free system is examined by reliability. The detection reliability is defined as the probability that a reader successfully detects the resonances of a chipless tag [10]. Figure 15 shows the testing scheme of the detection reliability. 36 IDs are selected, and they are readily transformed into the topology of the chipless tag. Afterward, these tags are fabricated, and their uncalibrated frequency signatures are measured. The results are output to Matlab, where an examination is conducted. The photograph of these test pieces is shown in Figure 16.

Figure 17 is the experimental setup in three environments. The 36 chipless tags are attached to a polystyrene foam sheet, a carton, and a plastic basket loaded with sundry items, respectively. The polystyrene foam is backed with an absorber, emulating a clutter-free environment, whereas the carton and the fully-loaded plastic basket are not. In particular, the carton is constructed by a 1.5-mm-thick paperboard, and the plastic basket is loaded with both conductive and non-conductive objects. In each scenario, the 36 chipless tags

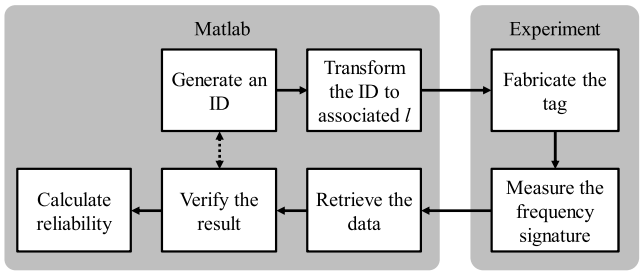

FIGURE 15. Flowchart for the test of noniterative design technique.

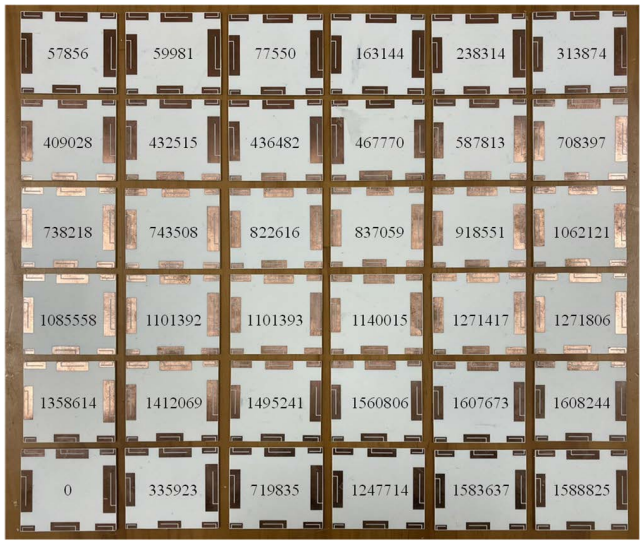

FIGURE 16. Photograph of the test pieces of chipless tags.

were tested over 3 read ranges, denoted by R, including $R = 10$ cm, $R = 15$ cm, and $R = 20$ cm. 10 measurements are repeatedly conducted at each distance. The measured results are evaluated as the read reliability along with the 95% confidence interval.

First of all, the capability of calibration-free signal processing is demonstrated in Figure 18. The coding information for the 10 selected IDs is shown in Table 2. The results include the proposed calibration-free technique and the calibrated normalized RCS, determined by

$$\sigma_{tag} = \left| \frac{S_{21(tag)} - S_{21(clutter)}}{S_{21(ref)} - S_{21(clutter)}} \right|^2 \times \sigma_{ref}, \tag{3}$$

where σ_{tag} is the RCS of the tag, $S_{21_{(tag)}}$ is the transfer function of the tag, $S_{21_{(clutter)}}$ is the transfer function of the background environment, $S_{21_{(ref)}}$ is the transfer function of a reference metallic surface, and σ_{ref} is the simulated RCS of the reference metallic surface. Using (3) requires performing two set of measurements, including the measurement of $S_{21_{(clutter)}}$ and that of $S_{21_{(tag)}}$. In contrast, the proposed technique requires performing only one set of measurement for $x(t)$. The resonances illustrated by the peaks are corresponding with the maxima of normalized RCS, suggesting the encoding can be successfully retrieved. In particular, the

TABLE 2. Arrangements for the resonant frequencies of IDs.

Resonances (GHz)	Index (i, j) for the IDs									
	57856	59981	77550	163144	313874	409028	837059	1101393	1560806	0
f_1^i	1 (2.000)	1 (2.000)	1 (2.000)	1 (2.000)	1 (2.000)	2 (2.045)	3 (2.091)	4 (2.139)	7 (2.287)	1 (2.000)
f_2^j	2 (2.249)	2 (2.249)	2 (2.249)	4 (2.353)	7 (2.516)	2 (2.249)	5 (2.406)	6 (2.460)	7 (2.516)	1 (2.224)
f_3^i	2 (2.691)	2 (2.691)	4 (2.815)	3 (2.752)	5 (2.879)	5 (2.879)	7 (3.011)	4 (2.815)	3 (2.752)	1 (2.632)
f_4^j	2 (2.961)	4 (3.096)	6 (3.238)	5 (3.167)	5 (3.167)	6 (3.238)	7 (3.312)	4 (3.096)	4 (3.096)	1 (2.895)
f_5^i	4 (3.705)	2 (3.542)	6 (3.875)	6 (3.875)	1 (3.464)	4 (3.705)	6 (3.875)	6 (3.875)	2 (3.542)	1 (3.464)
f_6^j	6 (4.262)	4 (4.075)	6 (4.262)	7 (4.359)	7 (4.359)	4 (4.075)	7 (4.359)	6 (4.262)	5 (4.168)	1 (3.810)
f_7^i	1 (4.559)	1 (4.559)	1 (4.559)	5 (4.986)	5 (4.986)	6 (5.099)	4 (4.876)	2 (4.662)	5 (4.986)	1 (4.559)
f_8^j	5 (5.485)	6 (5.609)	7 (5.736)	7 (5.736)	5 (5.485)	8 (5.867)	6 (5.609)	3 (5.244)	5 (5.485)	1 (5.014)

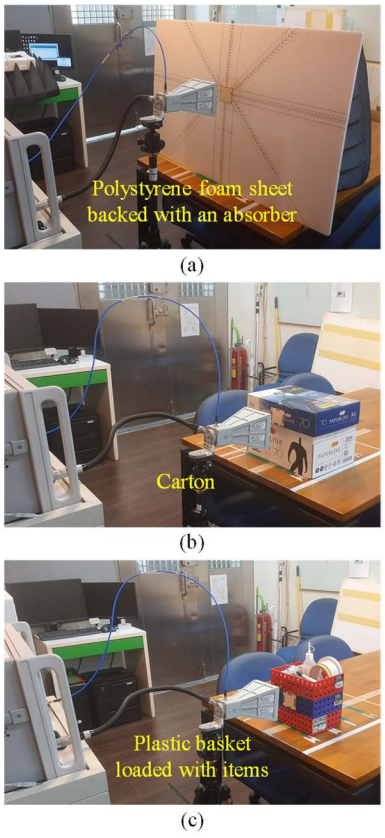

FIGURE 17. Experimental setups for the chipless tags attached to (a) a polystyrene foam sheet, (b) a carton, and (c) a plastic basket loaded with sundry items.

fourth sub-frequency band shows unclear maxima for the use of normalized RCS. The underlying reason at this band is an electrically-wider read range, which further reduces signal-to-noise ratio (SNR). Still, the results validate the calibration-free detection even for a 20.7-bit system.

Figure 19 presents the measured reliability for the tags attached to the polystyrene foam sheet. When $R = 10$ cm, the four bands depict average reliability of 100%, 95.0%, 98.3%, and 93.9%, respectively. Such high reliability indicates that the IDs are successfully transformed into the geometry of the tags. However, as the read range is extended to $R = 15$ cm, the average reliability is decreased as 96.7%, 93.1%, 47.2%, and 31.4%. The first and second bands preserve high reliability, whereas the third and fourth bands suffer from low SNR that degrades the reliability.

Next, the environment is modified as the carton, and the 36 (tags) $\times$ 10 (repeated tests) $\times$ 3 (read ranges) $=$ 1080 experiments were conducted. The reliability in this environment is illustrated in Figure 20. As compared to the clutter-free scenario, the carton causes slight frequency shifts for the chipless tags. While the reliability is still above 92.2% at the first two sub-frequency bands for $R = 10$ cm, the results are reduced as 81.3% and 72.9% at the third and fourth sub-frequency bands, respectively.

Finally, the environment is changed into the plastic basket loaded with the sundry items. The clutter responses are more significant than those in the previous scenarios. The measured reliability in this clutter-rich environment is shown in Figure 21. When $R = 10$ cm, the first and second sub-frequency bands still present reliability of 92.3% and 88.0%, respectively. The lowest reliability at this read range occurs at the fourth sub-frequency band (57.1%), indicating that large clutter responses and the loading effect deteriorate the detection. When the read range increases, low SNR reduces the reliability more notably. Considering the proposed system addresses a 20.7-bit system without implementing error correction codes, these results validate the proposed system for high SNR scenarios. Future research directions can integrate error correction codes [26], at the expense of data capacity, or assemble an array for each resonator to improve the SNR.

C. VALIDATION OF CALIBRATION-FREE SIGNAL PROCESSING

While the experimental results have validated the proposed 20.7-bit chipless RFID without iterative optimization or

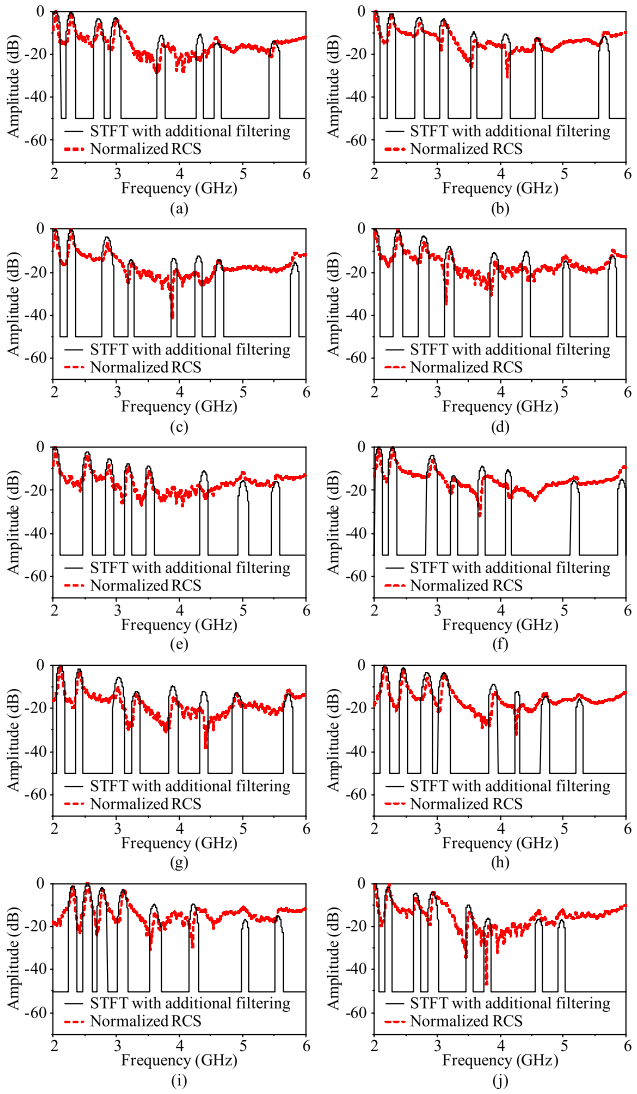

FIGURE 18. Measured results for the tags with IDs of (a) 57856, (b) 59981, (c) 77550, (d) 163144, (e) 313874, (f) 409028, (g) 837059, (h) 1101393, (i) 1560806, (j) 0.

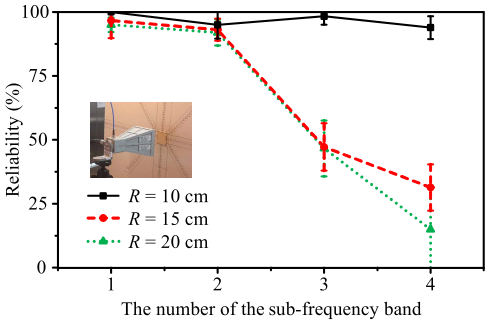

FIGURE 19. Measured reliability of the four sub-frequency bands for the tags attached to the polystyrene foam sheet.

additional calibration for the tag, the detection results may be dependent on the parameters in signal processing. Thus, the parameters in STFT are examined in terms of the reliability.

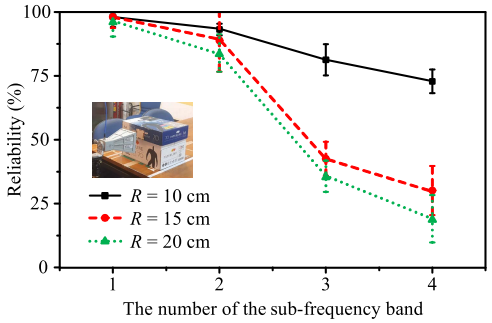

FIGURE 20. Measured reliability of the four sub-frequency bands for the tags attached to the carton.

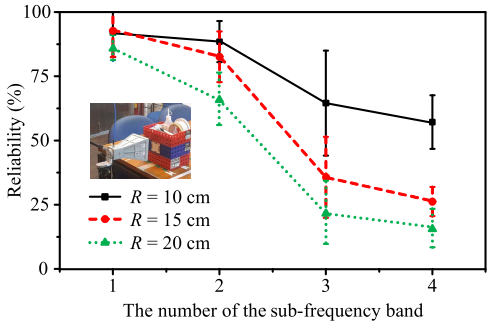

FIGURE 21. Measured reliability of the four sub-frequency bands for the tags attached to the plastic basket loaded with the sundry items.

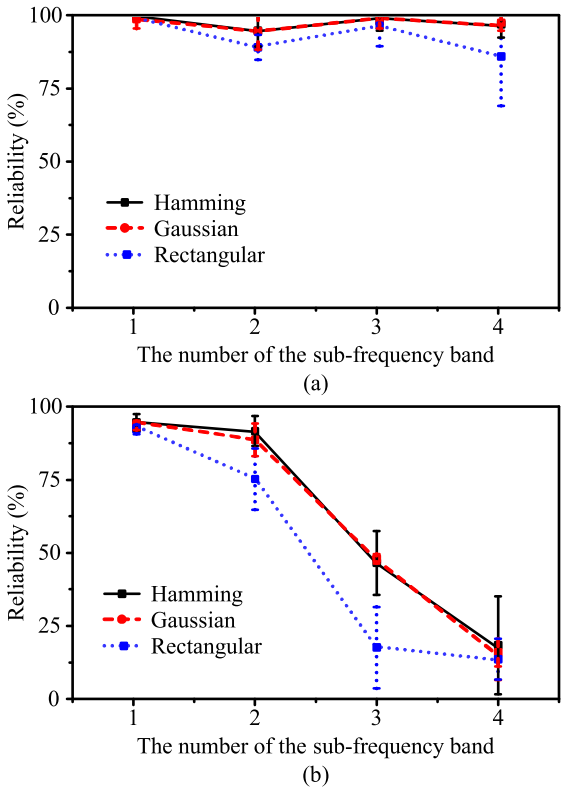

FIGURE 22. Comparison of the reliability for various window functions. (a) $R = 10$ cm. (b) $R = 20$ cm.

First, the window is varied over Hamming, Gaussian, and rectangular functions, $w(t)$, respectively. Following the

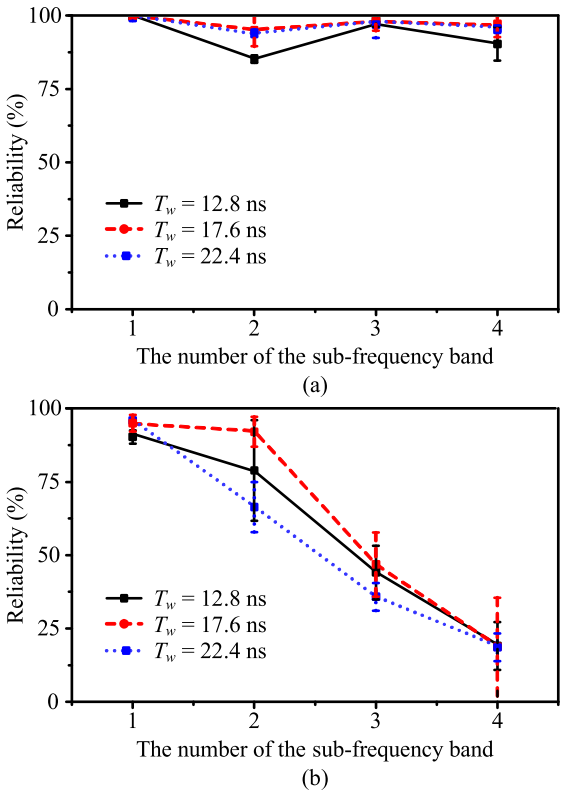

FIGURE 23. **Comparison of the reliability for various window lengths. (a) $R = 10$ cm. (b) $R = 20$ cm.**

experimental setup in Figure 17(a) and the evaluation scheme in Figure 15, the detection reliability with 95% of confident interval is presented in Figure 22. When $R = 10$ cm, the Hamming and Gaussian functions yield average reliability greater than 93%. No significant differences are found between the two windows. The rectangular window, on the other hand, causes lower reliability due to the blurred time-frequency spectrograms and confounding resonances. This situation becomes more severe when the SNR of the channel decreases, as can be seen in the result of $R = 20$ cm. Thus, the Hamming and Gaussian windows are more suitable to the STFT framework, despite the fact that the rectangular window is easy to be implemented and widely-used in the literature.

Next, the window length, T_w, is tested over three levels, including $T_w = 12.8$ ns, $T_w = 17.6$ ns, and $T_w = 22.4$ ns. Figure 23 demonstrates the measured reliability and the 95% of confident interval. These results echo with the time-frequency analysis shown in Figure 6. Insufficient window lengths incur overwhelming and unidentified magnitudes, which further cause aliasing of resonances, whereas excessive window lengths overly reduce magnitudes, especially at high resonant frequencies. Only the moderate window length ($T_w = 17.6$ ns) depicts the highest reliability at all the sub-frequency bands, as the magnitudes of time-frequency spectrogram balances the tradeoff between a resonant bandwidth and a sampling time. These results validate the parameterization using Hamming windows with $T_w = 17.6$ ns.

V. CONCLUSION

In this paper, a calibration-free and high-capacity chipless RFID system has been presented. As compared to the earlier calibration-free chipless RFID, the proposed system achieves the highest data capacity of 20.7 bits; more importantly, the 1.68 million chipless tags can be designed without iterative optimization using full-wave simulations, once the RSMs have been established. The noniterative design technique is validated by the R^2 of models, the residuals of prediction, and the reliability of measurement. The R^2 of the 8 RSMs is greater than 99%, and the residuals are confined to the average bandwidth of the frequency slots. The measured reliability of the four bands ranges from 93.9% to 100%. The proposed technique is expected to bridge the gap between the theoretical high-capacity chipless RFID and real-world applications with improved design efficiency.

REFERENCES

[1] M. M. Khan, F. A. Tahir, M. F. Farooqui, A. Shamim, and H. M. Cheema, "3.56-bits/cm 2 compact inkjet printed and application specific chipless RFID tag," *IEEE Antennas Wireless Propag. Lett.*, vol. 15, pp. 1109–1112, 2016.

[2] W. M. Abdulkawi and A.-F.-A. Sheta, "K-state resonators for high-coding-capacity chipless RFID applications," *IEEE Access*, vol. 7, pp. 185868–185878, 2019.

[3] F. Babaeian and N. Karmakar, "Compact multi-band chipless RFID resonators for identification and authentication applications," *Electron. Lett.*, vol. 56, no. 14, pp. 724–727, Jul. 2020.

[4] M. Khaliel, A. El-Awamry, A. F. Megahed, and T. Kaiser, "A novel design approach for co/cross-polarizing chipless RFID tags of high coding capacity," *IEEE J. Radio Freq. Identificat.*, vol. 1, no. 2, pp. 135–143, Jun. 2017.

[5] M. Pöpperl, A. Parr, C. Mandel, R. Jakoby, and M. Vossiek, "Potential and practical limits of time-domain reflectometry chipless RFID," *IEEE Trans. Microw. Theory Techn.*, vol. 64, no. 9, pp. 2968–2976, Sep. 2016.

[6] C. Herrojo, F. Paredes, J. Bonache, and F. Martin, "3-D-printed high data-density electromagnetic encoders based on permittivity contrast for motion control and chipless-RFID," *IEEE Trans. Microw. Theory Techn.*, vol. 68, no. 5, pp. 1839–1850, May 2020.

[7] F. Babaeian and N. C. Karmakar, "Hybrid chipless RFID tags—A pathway to EPC global standard," *IEEE Access*, vol. 6, pp. 67415–67426, 2018.

[8] Y.-Z. Ni, X.-D. Huang, Y.-P. Lv, and C.-H. Cheng, "Hybrid coding chipless tag based on impedance loading," *IET Microw., Antennas Propag.*, vol. 11, no. 10, pp. 1325–1331, Aug. 2017.

[9] Y.-S. Chen, T.-Y. Jiang, and F.-P. Lai, "Automatic topology generation of 21 bit chipless radio frequency identification tags using a noniterative technique," *IEEE Antennas Wireless Propag. Lett.*, vol. 18, no. 2, pp. 293–297, Feb. 2019.

[10] J.-A. Lin, J.-Y. Jhang, F.-P. Lai, B.-L. Lin, Y.-M. Jhang, and Y.-S. Chen, "Analysis of calibration-free detection techniques for frequency-coded chipless RFID," *IEEE Trans. Antennas Propag.*, vol. 69, no. 3, pp. 1681–1691, Mar. 2021.

[11] A. Ramos, E. Perret, O. Rance, S. Tedjini, A. Lázaro, and D. Girbau, "Temporal separation detection for chipless depolarizing frequency-coded RFID," *IEEE Trans. Microw. Theory Techn.*, vol. 64, no. 7, pp. 2326–2337, Jul. 2016.

[12] A. Ramos, Z. Ali, A. Vena, M. Garbati, and E. Perret, "Single-layer, flexible, and depolarizing chipless RFID tags," *IEEE Access*, vol. 8, pp. 72929–72941, 2020.

[13] Z. Ali, E. Perret, N. Barbot, and R. Siragusa, "Extraction of aspect-independent parameters using spectrogram method for chipless frequency-coded RFID," *IEEE Sensors J.*, vol. 21, no. 5, pp. 6530–6548, Mar. 2021.

[14] R. Tavares de Alencar, Z. Ali, N. Barbot, M. Garbati, and E. Perret, "Practical performance comparison of 1-D and 2-D decoding methods for a chipless RFID system in a real environment," *IEEE J. Radio Freq. Identificat.*, vol. 4, no. 4, pp. 532–544, Dec. 2020.

[15] J.-W. Hsu, F.-P. Lai, and Y.-S. Chen, "Calibration-free chipless radiofrequency identification tags with enhanced data capacity," in *Proc. IEEE Asia–Pacific Microw. Conf. (APMC)*, Dec. 2019, pp. 1–3.
[16] S. Genovesi, F. Costa, F. A. Dicandia, M. Borgese, and G. Manara, "Orientation-insensitive and normalization-free reading chipless RFID system based on circular polarization interrogation," *IEEE Trans. Antennas Propag.*, vol. 68, no. 3, pp. 2370–2378, Mar. 2020.
[17] F. Costa, S. Genovesi, and A. Monorchio, "Normalization-free chipless RFIDs by using dual-polarized interrogation," *IEEE Trans. Microw. Theory Techn.*, vol. 64, no. 1, pp. 310–318, Jan. 2016.
[18] J. Aliasgari and N. C. Karmakar, "Mathematical model of chipless RFID tags for detection improvement," *IEEE Trans. Microw. Theory Techn.*, vol. 68, no. 10, pp. 4103–4115, Oct. 2020.
[19] J. Kracek, M. Svanda, and K. Hoffmann, "Scalar method for reading of chipless RFID tags based on limited ground plane backed dipole resonator array," *IEEE Trans. Microw. Theory Techn.*, vol. 67, no. 11, pp. 4547–4558, Nov. 2019.
[20] J. Aliasgari and N. C. Karmakar, "A pulse distortion approach for decoding frequency-coded tags in multicarrier chipless RFID systems," *IEEE Trans. Microw. Theory Techn.*, vol. 70, no. 3, pp. 1856–1870, Mar. 2022.
[21] G. Khadka, M. A. Bibile, L. M. Arjomandi, and N. C. Karmakar, "Analysis of artifacts on chipless RFID backscatter tag signals for real world implementation," *IEEE Access*, vol. 7, pp. 66821–66831, 2019.
[22] F. Gillon and P. Brochet, "Screening and response surface method applied to the numerical optimization of electromagnetic devices," *IEEE Trans. Magn.*, vol. 36, no. 4, pp. 1163–1167, Jul. 2000.
[23] Y.-S. Chen, T.-Y. Jiang, and F.-P. Lai, "Design rule development for frequency-coded chipless radiofrequency identification with high capacity," *IET Microw., Antennas Propag.*, vol. 13, no. 8, pp. 1255–1261, Jul. 2019.
[24] G. Abgaryan and D. Tumakov, "Designing a koch-type wire antenna by regression analysis," in *Proc. IEEE East-West Design Test Symp. (EWDTS)*, Sep. 2018, pp. 1–4.
[25] B. Liu, M. O. Akinsolu, C. Song, and Q. Hua, "An efficient method for complex antenna design based on a self adaptive surrogate model-assisted optimization technique," *IEEE Trans. Antennas Propag.*, vol. 69, no. 4, pp. 2302–2315, Apr. 2021.
[26] G. Khadka, M. S. Arefin, and N. C. Karmakar, "Using punctured convolution coding (PCC) for error correction in chipless RFID tag measurement," *IEEE Microw. Wireless Compon. Lett.*, vol. 30, no. 7, pp. 701–704, Jul. 2020.

JIA-WEN HSU was born in Kaohsiung, Taiwan, in 1996. He received the B.S. degree in telecommunication engineering from the National Kaohsiung University of Science and Technology, Kaohsiung, in 2018, and the M.S. degree in electronic engineering from the National Taipei University of Technology (NTUT), in 2020.

He joined the EM Optimization Laboratory, NTUT, from 2018 to 2020, as a Research Assistant, working on the signal processing of chipless RFID. Since 2021, he has been with Sercomm Corporation, Taipei, Taiwan, as an RF Engineer. He is responsible for the research and development of LTE/5G CPE, verifying RF performance of products, and providing technical supports to customers.

FEI-PENG LAI was born in Chiayi, Taiwan. She received the B.S. degree in electronic engineering from the National Taipei University of Technology, in 2017, where she is currently pursuing the Ph.D. degree in electronic engineering. Her current research interests include chipless RFID, antennas, and wireless communications. She has participated in numerous research projects, including 60-GHz on-chip antennas from KaiKuTek, Taiwan, and chipless RFID development from the Ministry of Science and Technology, Taiwan. She has served on the reviewer board for the IEEE Access.

YEN-SHENG CHEN (Member, IEEE) was born in Taichung, Taiwan. He received the B.S. degree in electrical engineering and the M.S. and Ph.D. degrees in communication engineering from the National Taiwan University, Taipei, Taiwan, in 2007, 2009, and 2012, respectively.

Since 2013, he has been a Faculty Member with the Department of Electronic Engineering, National Taipei University of Technology (NTUT), Taipei, where he is currently a Professor. He has participated in a wide range of research projects, including chipless RF identification, transparent antennas and metasurfaces, mm-wave antennas and circuits, RF energy harvesting, antenna array failure correction, antennas for body centric communications, microwave reconfigurable components, and multiobjective optimization techniques. His current research interests include chipless sensor networks, high-gain antennas, and inkjet printing technology.

Dr. Chen was a recipient of the Outstanding Reviewers Award from the IEEE Antennas and Wireless Propagation Letters, from 2017 to 2021, the Outstanding Reviewers Award from the IEEE Transactions on Antennas and Propagation, in 2019 and 2020, respectively, the Future Tech Award from the Ministry of Science and Technology, Taiwan, in 2021, the Outstanding Research Award from the NTUT, in 2019, the Dr. Shechtman Young Researcher Award from the NTUT, in 2018, the Outstanding Research Award from the College of Electrical Engineering and Computer Science (EECS), NTUT, in 2018 and 2019, respectively, and the Remarkable Teaching Award from the College of EECS, NTUT, in 2020. He was the General Secretariat and Publication Chair for ISAP 2021 Symposium and the Guest Editor of *IEICE Communications Express*, in 2022. He has served on the editorial/review boards for many technical journals, transactions, proceedings, and letters.